

Mechanism of an Exceptional Class of Photostabilizers: A Seam of Conical Intersection Parallel to Excited State Intramolecular Proton Transfer (ESIPT) in *o*-Hydroxyphenyl-(1,3,5)-triazine

Martin J. Paterson,^{†,||} Michael A. Robb,^{*,†} Lluís Blancafort,[‡] and Anthony D. DeBellis[§]

Department of Chemistry, Imperial College London, London, SW7 2AZ, United Kingdom, Institut de Química Computacional, Departament de Química, Universitat de Girona, Campus de Montilivi, 17071 Girona, Spain, and Ciba Specialty Chemicals, Coating Effects Research Department, 540 White Plains Road, Tarrytown, New York 10591

Received: March 3, 2005; In Final Form: June 7, 2005

We present a detailed CASSCF study of the mechanism of excited-state intramolecular proton transfer (ESIPT) in the *o*-hydroxyphenyl triazine class of photostabilizers. The valence-bond analysis of the ground state and the two $\pi\pi^*$ excited states permits a simple chemical interpretation of the mechanistic information. Our results show that the barrier to enol–keto tautomerism on the ground-state adiabatic surface is high. Following photoexcitation to the charge-transfer state, the ESIPT is predicted to take place without a barrier. Radiationless decay to the ground state is associated with an extended seam of conical intersection, with a sloped topology lying parallel to the ESIPT path, which can be accessed at any point along the reaction path. Our results show that the triazine class of photostabilizers has the photochemical and photophysical qualities associated with exceptional photostability.

Introduction

Ultraviolet (UV) light (in the range of 300–400 nm) can degrade polymeric materials via a variety of chemical mechanisms.¹ To prevent destructive degradation of such materials, a means of removing the absorbed radiation is required. The absorbed energy must be removed on an ultrafast (subpicosecond) time scale, before the material can degrade via some reactive product channel.

To this end, UV absorbers have been developed as compounds that are added as coatings to polymeric products. The UV absorbers (or light stabilizers) filter off the radiation via an internal conversion mechanism and return to the ground electronic state on a subpicosecond time scale. We have recently shown for the benzotriazole (BZT) class of UV absorbers that a conical intersection between the ground and the first excited singlet state is responsible for the ultrafast internal conversion mechanism.² In BZT, a proton-transfer coupled to an electron transfer is the excited-state reaction responsible for the system reaching the conical intersection on the S_1 adiabatic surface.

The potential energy surface topology in the region of a conical intersection is the central feature that determines photostability. We shall discuss two contrasting general situations. The classic picture of a conical intersection funnel in photochemistry is shown in Figure 1. The model here is like sand in a funnel. The second possibility is shown in Figure 2 and corresponds to the situation where the reaction path is

approximately parallel to the seam of the intersection. We now discuss these possibilities and how they relate to photostability (see ref 3 for a mathematical discussion of the various first-order conical intersection topologies).

We begin by discussing the classical situation for radiationless decay involving a funnel type conical intersection as shown in Figure 1. This type of conical intersection is called peaked. Notice that there are two directions labeled x_1 (gradient-difference) and x_2 (derivative-coupling) that define the branching space, which lifts the degeneracy at first-order in nuclear displacements. There are two important mechanistic points to make concerning this figure. First, decay at such a conical intersection, in general, leads to new chemical species corresponding to photodegradation and is thus undesirable. Thus, it can easily be seen that on exiting from the upper sheet of the double-cone onto the ground-state potential energy surface, one could go in the forward direction and generate a new photochemical product or one could come out of the funnel in the opposite direction regenerating the reactant. Even if the quantum yield of a new photoproduct is small, over many ($>10^{15}$) photocycles, the stabilizer can begin to degrade. The second point relates to the fact that the reaction path itself lies in the funnel (branching space), hence the sand flowing through the funnel analogy. The second example, which we shall now consider, is distinguished by the fact that the reaction path does not lie in the branching space.

Now let us consider the conical intersection topology shown in Figure 2. In this case, the potential energy surface is plotted using one coordinate vector from the branching space and a reaction coordinate. The conical intersection, in this representation, appears as a seam. Thus, the reaction path lies approximately parallel to the seam of the conical intersection. If one takes a cut along the branching space coordinate, a conical intersection appears as sloped (see inset to right of Figure 2). From a mechanistic point of view, the situation is very different

* Corresponding author. E-mail: mike.robb@imperial.ac.uk.

[†] Department of Chemistry, Imperial College London, London, SW7 2AZ, United Kingdom.

[‡] Institut de Química Computacional, Departament de Química, Universitat de Girona, Campus de Montilivi, 17071 Girona, Spain.

[§] Ciba Specialty Chemicals, Coating Effects Research Department, 540 White Plains Road, Tarrytown, New York 10591.

^{||} Current address: Department of Chemistry, University of Århus, DK-8000 Århus C, Denmark.

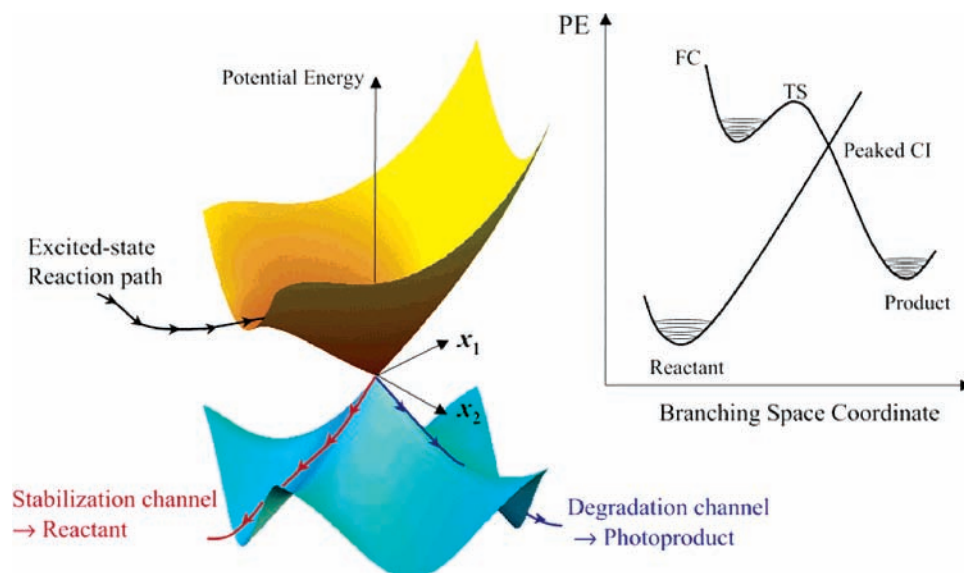


Figure 1. Generic peaked conical intersection topology. The intersection is a funnel on the reaction path, and the reaction can branch to either the reactants or the photoproducts. Thus, a peaked topology provides at least one degradation channel (blue) in addition to a stabilization channel (red).

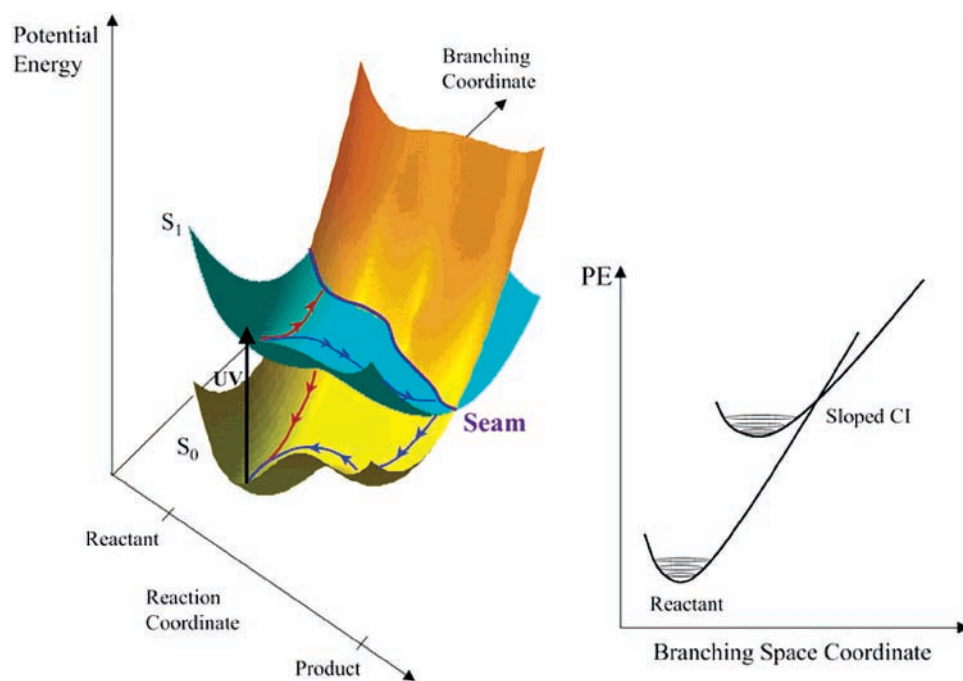


Figure 2. Generic potential surfaces exhibiting a seam of conical intersections with a first-order sloped topology. The reaction path lies parallel to the seam. There are two possible decay pathways: (i) an adiabatic reaction followed by decay in the product region (blue path) and (ii) decay at the reactant side (red path). The preferred path will depend on various barrier heights and the orientation of the reaction path relative to the seam.

from the sand in the funnel model. The conical intersection line is reached by nuclear motion orthogonal to the reaction path. Clearly, if this intersection line is accessed in the region of the reactants, the only possibility is photophysical regeneration of the reactant (red path in Figure 2), and this is the ideal paradigm for photostability. On the other hand, one may have an adiabatic photochemical transformation on S_1 , and the seam is only accessed on the product side (blue path in Figure 2). In this case, photostability only occurs if the barrier on the ground state, in the direction of the reactants, is negligible and if the barrier toward other possible chemical species is prohibitively large. Finally, we should mention that if one has a peaked conical intersection of the form shown in Figure 1, then the outcome of the photochemistry also depends on the position of the funnel along the reaction coordinate and the presence of ground-state

reaction barriers toward regeneration of the reactants and the formation of new chemical species.

It is now clear what the optimum topology of the potential surface must be for an efficient photostabilizer. In general, a reaction path that proceeds via a peaked intersection, shown in Figure 1, always leads to at least one new chemical species (as well as reactant regeneration on the ground-state potential surface), unless there are barriers on the ground state surface. In contrast, the potential energy surface topology in Figure 2, where the reaction path lies approximately parallel to the conical intersection line, provides a viable mechanism for photostabilization. If decay occurs on the reactant side, where the conical intersection is sloped, reactant regeneration occurs. If decay occurs on the product side, then a new chemical species is generated, and the system is photostable only if the barrier on

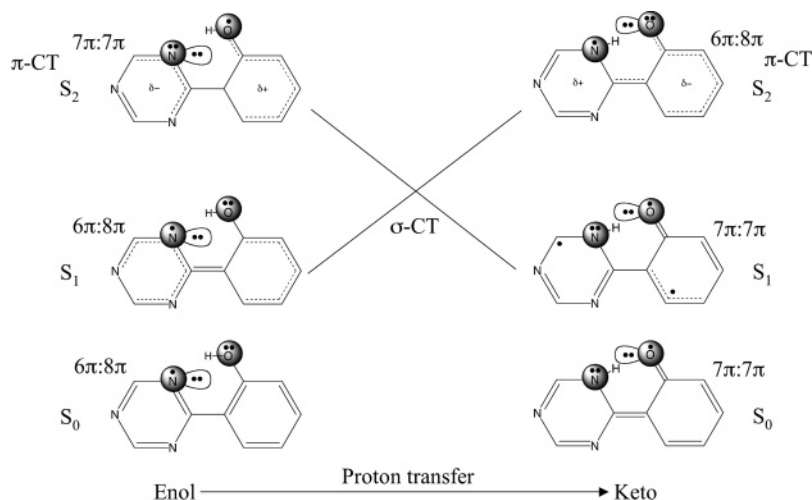
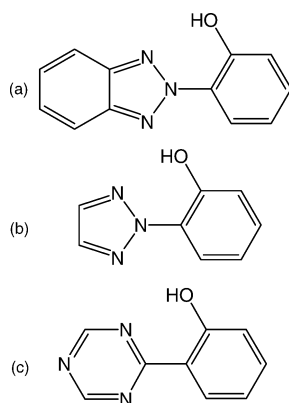


Figure 3. State correlation diagram along proton-transfer reaction coordinate. The enol S_2 state is a CT state in which the electron density is transferred from the phenyl to the triazine ring and correlates diabatically with the covalent S_1 keto state, where the σ -electron density is transferred in the opposite direction to balance the charge. The situation is analogous for the S_2 keto and S_1 enol states.

CHART 1: (a) *o*-Hydroxyphenyl Benzotriazole (BZT) Photostabilizer, (b) BZT Model Studied Previously in Ref 2, and (c) *o*-Hydroxyphenyl-(1,3,5)-triazine Investigated in the Current Study



the ground state is small enough so that reactant regeneration can occur. Clearly, for a good photostabilizer, one also wants the minimum nuclear motion possible before reactant regeneration occurs at a sloped conical intersection. Thus, the topology shown in Figure 2 represents the design objective for a photostabilizer because decay can occur at any point on the reaction path.

In this paper, we shall discuss the mechanism of action of the class of *o*-hydroxyphenyl-triazine UV absorbers, which are known to be very efficient photostabilizers.⁴ This system chemically appears very similar to the BZT class we have previously studied.² However, as we shall discuss, the valence-bond nature of the excited states is quite different. The triazines differ from BZT mainly in the size of the nitrogen heterocycle hydrogen bonded to the phenolic group. It has been reported that the intramolecular hydrogen bond in the ground state for the *o*-hydroxyphenyl-triazines is stronger than that in BZT.⁵ In BZT, the triazole ring is five-membered, while triazine is six-membered (see Chart 1). It is this factor that appears to be crucial in understanding the differences in the photostability mechanisms of both species. In BZT, it is the $n\pi^*$ -state that is relevant, where as in triazines, the $\pi\pi^*$ -states are the main players. In both molecular systems, the photostabilization is associated with regeneration following an excited-state intramolecular proton transfer (ESIPT). However, as we shall subsequently discuss, the two systems differ in the nature of the excited states involved

and in the details of the geometrical changes along the reaction path. These effects will yield an explanation of why the *o*-hydroxyphenyl-triazines are generally more photostable, as a class, than their *o*-hydroxyphenyl-benzotriazole counterparts.⁶

In Chart 2, we show the range of triazine systems that had been studied experimentally. With preliminary TD-DFT calculations, we have explored the nature of the low-lying excited states. Our objective was to identify any similarities and differences based on the azine chromophores. Our computations showed that the chemical nature of the first two $\pi\pi^*$ -states is similar for all chromophores and that the vertical excitation energies all lie in the same energy range, although the ordering of the two $\pi\pi^*$ -states varies depending on the chromophore. Thus, we have chosen *o*-hydroxyphenyl-(1,3,5)-triazine (R^1 in Chart 2) and *o*-hydroxyphenyl-(1,2,4)-triazine (R^4 , R^5 , and R^6 in Chart 2) as the model systems for detailed excited-state reaction path exploration. In this paper, we shall discuss only the results for *o*-hydroxyphenyl-(1,3,5)-triazine since those for *o*-hydroxyphenyl-(1,2,4)-triazine are almost identical from a mechanistic point of view (i.e., the valence-bond analysis of the states is identical, and the optimized conical intersections are found to have similar geometries and energetics).

Now, let us consider the nature of the excited states involved in the photostabilizer properties of triazines. In the triazines, there are three states involved, the ground state and two $\pi\pi^*$ -states. We shall now discuss the correlation of the excited-state manifolds of the enol and keto forms of *o*-hydroxyphenyl-(1,3,5)-triazine. A valence-bond representation of the states involved at the enol and keto geometries is shown in Figure 3. These figures have been constructed from the analysis of the computed CASSCF wave functions. The enol to keto transformation involves essentially an H^+ migration from the hydroxyphenyl O atom to the triazine N atom, a three-orbital four-electron rearrangement of the σ -system, and there is no net electron transfer in the σ -system. In the π -electron system, in the ground-state enol form, the triazine moiety has six π -electrons, and the *o*-hydroxy fragment has eight π -electrons. We shall use the notation $6\pi:8\pi$ to describe this situation. However, we note that this notation is only approximate and is based on the partial charge distribution of the vertically excited enol and keto species. In the ground-state keto form, the π -electron arrangement can be denoted $7\pi:7\pi$. At the enol and keto geometries, there are two different types of $\pi\pi^*$ -states: a locally excited state (LE) and a charge transfer state (CT). The locally

excited state is a valence tautomer of the (enol or keto) ground state. At both enol and keto geometries, the lowest energy excited-state S_1 is LE, and the higher energy excited-state S_2 is CT. Thus, at the enol geometry, the S_0 and S_1 states are both $6\pi:8\pi$, while the S_2 (CT) state is $7\pi:7\pi$. One has the analogous situation at the keto geometry. The most important observation to be made is that the $7\pi:7\pi$ enol S_2 (CT) state correlates diabatically with the $7\pi:7\pi$ keto S_1 (LE) state as indicated in Figure 3. In a similar fashion, the $6\pi:8\pi$ enol S_1 (LE) state correlates directly with the $6\pi:8\pi$ keto S_2 (CT) state.

There is one additional important point that arises from the consideration of the VB structures and the correlation diagram shown in Figure 3. If we consider the enol or keto form, or indeed any geometry along the reaction coordinate (H migration), one can observe that the VB structures for S_0 , S_1 , and S_2 differ only in the couplings of the π -electrons. The couplings of the σ -electrons are unchanged. Thus, the nuclear motion that couples S_0 to S_1 must involve only the skeletal framework, not hydrogen motion. It follows from this that the branching space coordinates will not involve hydrogen motion and can only involve skeletal deformation. Thus, whether we are considering an S_0/S_1 seam of crossing or an S_2/S_1 seam of crossing, the branching space coordinates must be skeletal deformations since these are the motions that couple the VB states. Accordingly, the surface crossings will be of the sloped variety, all along the reaction coordinate, similar to the cartoon shown in Figure 2 (see refs 7 and 8 for examples of this conical intersection topology, accessible via skeletal deformation).

The nature of the optically allowed absorption is also clear from Figure 3. The allowed transition must involve charge transfer to have an appreciable oscillator strength. Thus, for the enol form, the optical absorption must involve excitation to S_2 (i.e., $6\pi:8\pi$ to $7\pi:7\pi$). However, this excited state, in turn, correlates directly with the corresponding keto S_1 LE state. Thus, elementary VB ideas suggest that the excited-state transformation from enol to keto will proceed (diabatically) without a barrier on the $7\pi:7\pi$ potential surface (possibly via an S_2/S_1 conical intersection).

Experimentally, in both BZT and triazine, it is the CT state that is populated following optical absorption. In *o*-hydroxyphenyl-(1,3,5)-triazine, the state ordering between the LE state and the CT state is difficult to determine unambiguously since the states are very close together at both CASSCF and TD-DFT levels. In the previous BZT study, the state ordering was also difficult to assign; however, optimized reaction channels on the S_1 adiabatic surface were found for both states. The situation for triazine is similar. The optical absorption is to the CT state, which comes out as S_2 in the CASSCF computations. Because of the ambiguity of the order of the states at the theoretical level, our objective is to document optimized reaction pathways and places where radiationless deactivation can occur and then interpret these data in a manner independent of the ordering of the CT or LE states.

To conclude this section, we would like to summarize the basic features of the potential surface that emerges from our computations (see the cartoon in Figure 4) and briefly indicate the central mechanistic scenario that emerges. We emphasize that the qualitative features of the potential surface are predictable from the VB structures shown in Figure 3. The most important point is that the S_0 and S_1 VB structures differ only in the coupling of the π -electrons. Thus, the branching space coordinates that couple the states must involve skeletal motion, while the reaction coordinate is H-transfer. Accordingly, the intersection region between S_0 and S_1 will have a topology

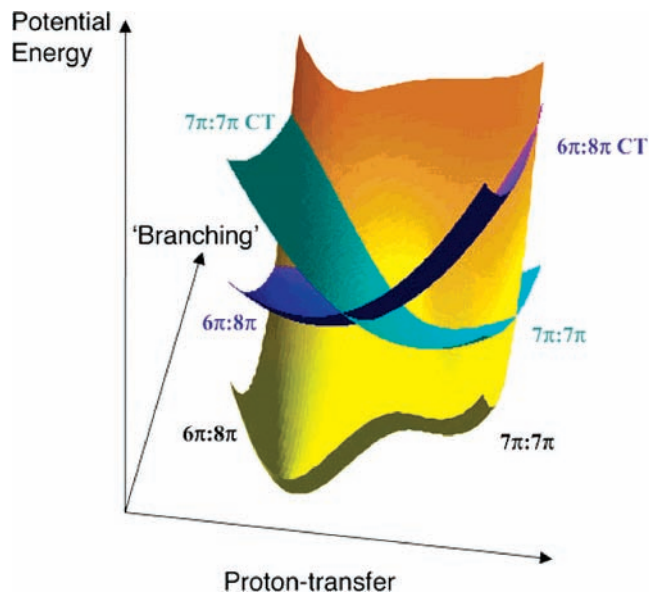


Figure 4. Schematic representation of the potential surfaces for the triazine ESIPT reaction. The light blue diabatic state is the optically excited CT state, which crosses with the neutral excited keto diabatic state (dark blue).

similar to that shown in Figure 2 with a sloped conical intersection all along the reaction path. Indeed, as indicated in Figure 4, at the keto side, we have been able to optimize a sloped conical intersection K_{CI} adjacent to the minimum. The conical intersection is easily accessible, some 5 kcal mol⁻¹ above the planar S_1 keto minimum. Similarly, one can optimize an enol S_0/S_1 conical intersection E_{CI} . We have also been able to locate S_1/S_0 surface crossings near the transition state connecting E^* and K^* , the S_1 excited state minima. Thus, the central point, which we will elaborate on subsequently, is that one has verified computationally that the S_1/S_0 surface topology has the form shown in Figure 2. From a mechanistic point of view, it is clear that after decay at the keto side, the system can then easily convert back to the enol form due to the very small ground-state barrier.

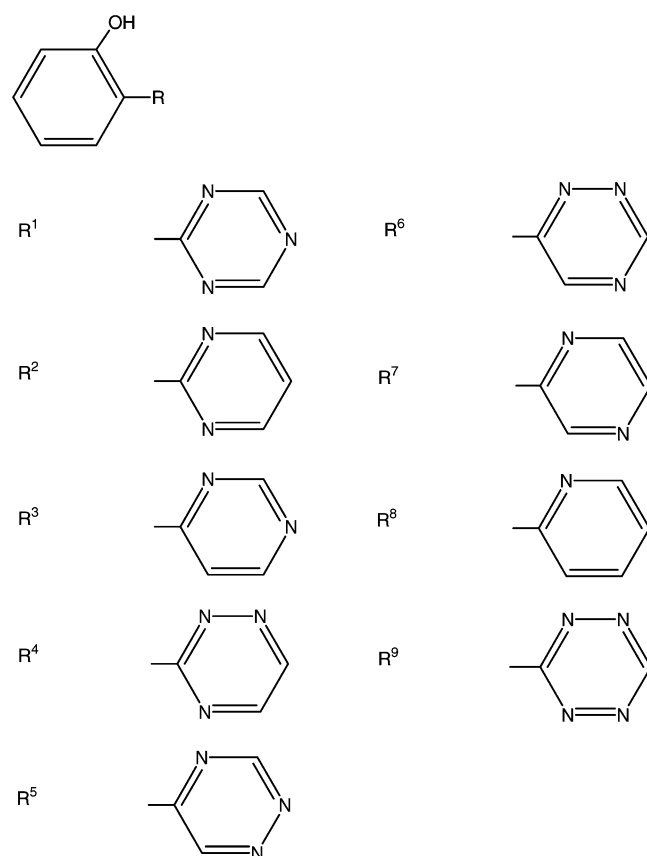
The remaining issue to discuss in relation to Figure 4 concerns the deactivation from S_2 to S_1 . Again, since at any geometry along the reaction coordinate the VB structures for S_1 and S_2 differ only in the couplings of the π -electrons, one can predict an extended S_1/S_2 seam of intersection along the H migration coordinate. We have in fact optimized an S_2/S_1 conical intersection, which we will discuss subsequently. However, at this stage, we reiterate again the fact that the S_2 charge-transfer state at the enol geometry correlates diabatically with the S_1 locally excited state at the keto geometry. Thus, one predicts barrierless motion from the S_2 enol structure to the S_1 keto geometry from which facile decay is possible.

Computational Details

In this study, we have used complete active space self-consistent field (CASSCF) formalism to compute the ground- and excited-state potential energy surfaces for both *o*-hydroxyphenyl-(1,3,5)-triazine and *o*-hydroxyphenyl-(1,2,4)-triazine. Computations were carried out with a development version of the *Gaussian*⁹ program, using a 6-31G* basis. The choice of active space and the methodologies for the wave function analysis are discussed next.

The excited-state wave functions in the vertical excitation region were compared against time-dependent density-functional

CHART 2



theory (TDDFT),¹⁰ using the B3LYP functional. In addition, we have used TDDFT to study the vertically excited states in a series of six-membered nitrogen containing *o*-hydroxyphenyl derivatives (see Chart 2).

Exploratory computations showed that the $\pi\pi^*$ -excited states are responsible for the ultrafast deactivation; thus, the active space was constructed based on these states. The full π -electron space consists of the 14 π -electrons distributed in all possible ways in the 13 p_{π} molecular orbitals. This generates 1 473 186 configurations. Computations at this level with gradient optimization of the geometry are very expensive, and this active space was only used for single-point energy computations. To generate reduced active spaces, quasi-occupied and -virtual orbitals were removed from the active space window on the basis of the diagonal elements of the reduced one-electron density matrix from a CAS(14,13) computation. In the ground state and first two excited states, at least one orbital had an occupation number greater than 1.99; therefore, this orbital was then discarded from the active space. Similarly, at least one orbital had an occupation number of 0.001, and this orbital was also discarded. The removal of this pair of orbitals gave a (12,-11) active space, generating 106 953 configurations, and this active space was used to explore the potential surfaces of the ground and first two $\pi\pi^*$ -excited states. The CAS(12,11) computations were checked against single-point CAS(14,13) computations by examining the vertical excitation energies from both active spaces and comparing the excited-state wave functions.

While the (12,11) active space was used for the majority of geometry optimizations, a further reduction was necessary to perform analytical frequency computations. From the (12,11) active space, a further quasi-occupied and two further quasi-virtual orbitals were removed to give a (10,8) active space

generating 1176 configurations. At minima on the ground and excited surfaces, the (10,8) active space was used to reoptimize geometries, which had previously been optimized using the (12,-11) active space. In this manner, the characterization of the optimized critical points as minima or saddle points was obtained from the subsequent frequency computation. However, all optimized geometries are quoted for the (12,11) active space.

For transition states, the (10,8) active space was used for the optimization since analytical second derivatives were required at each point of the optimization to prevent collapse to a minimum. The (12,11) active space energies were then recomputed by a single-point energy computation at the (10,8) active space optimized geometries.

For conical intersection optimizations, the (12,11) active space was used. These were optimized approximately, neglecting the orbital rotation derivatives. Neglecting these terms has been shown to give a negligible effect on optimized conical intersection geometries. We have verified this by (fully) reoptimizing the keto conical intersection with the (10,8) active space and observing only small changes to the geometry, gradient difference, and derivative coupling vectors. Similarly, we have neglected the orbital rotation derivatives in optimizing excited-state minima using state-averaged gradients.

The valence-bond analysis of the ground and excited states was carried out using the full (14,13) active space. The VB structures were obtained using the spin-exchange density (P_{ij}) computed with localized active orbitals obtained with the Boys method.¹¹ The details of this method have been described elsewhere.¹² As we have discussed elsewhere,^{2,13} the P_{ij} matrix elements have a simple interpretation that allows one to assign the interatomic spin-coupling and thus draw the VB resonance structures. For a single configuration, perfectly paired valence bond (VB) wave function, the P_{ij} have values of +1 for a singlet-coupled pair, -1 for a triplet-coupled pair, and -1/2 when the pair is uncoupled. From a practical point of view, the P_{ij} elements for neighboring atoms give an idea of the π -bonding (i.e., π -bond localization in the different structures). Configuration interaction and charge-transfer configurations mean that the actual computed values differ from these idealized values. In our experience, values >0.4 are a sign of localized double bond character. Moreover, changes with respect to the ground state can be understood as a decrease or increment in the bond order due to the excitation.

We note that the P_{ij} values are particularly useful in situations where there are clear bonding patterns (e.g., the keto side of the photochemical reaction studied here), although their interpretation is difficult in situations of delocalized bonding (e.g., the enol side). Thus, the ground-state enol form has a significant aromatic character in both rings, and the S_1 and S_2 excitations induce a general decrease of the bonding. In contrast to this, the ground-state keto tautomer has a localized bonding pattern, and the S_1 excitation induces an inversion in the conjugated π -system formed by the C₃, N₄, C₅, N₆, C₁, and C_{1'} atoms (see the changes of the P_{ij} elements in Table 5).

Finally, we consider the diagonal elements of the one-electron density matrix D_{ii} , calculated with localized active space orbitals. They give the occupations of the π -orbitals and are useful to assess the charge-transfer character of the various states. The $8\pi:6\pi$ notation used to describe this character is only approximate and does not consider the P_{ij} elements that change as the hydrogen atom is transferred.

Results and Discussion

We have computed the vertical excitation spectra for the series of compounds shown in Chart 2. The results and chemical

TABLE 1: TDDFT Vertical Excitation Energies for Several *o*-Hydroxyphenyl Nitrogen Heterocycles as Shown in Chart 2 (TD-B3LYP/6-31G*)

state	R ¹	R ²	R ³	R ⁴	R ⁵	R ⁶	R ⁷	R ⁸	R ⁹
S ₁	A' 3.59 eV (0.1030) $\pi\pi^*$ CT (Ph \rightarrow Tri)	A' 3.69 eV (0.0023) $\pi\pi^*$ CT (Ph \rightarrow Tri)	A' 3.70 eV (0.1410) $\pi\pi^*$ CT (Ph \rightarrow Tri)	A' 3.03 eV (0.0054) $\pi\pi^*$ CT (Ph \rightarrow Tri) HOMO \rightarrow LUMO	A'' 3.11 eV (0.0034) $n\pi^*$ (n_N anti \rightarrow LUMO deloc.)	A' 3.16 eV (0.0134) $\pi\pi^*$ CT (Ph \rightarrow Tri) HOMO \rightarrow LUMO	A' 3.53 eV (0.0795) $\pi\pi^*$ CT (Ph \rightarrow Tri) Tri HOMO \rightarrow LUMO	A' 3.82 eV (0.1580) $\pi\pi^*$ CT (Ph \rightarrow Tri) Tri HOMO \rightarrow LUMO	A'' 2.20 eV (0.0041) $n\pi^*$ (n_N anti \rightarrow LUMO localized)
S ₂	A' 3.81 eV (0.0002) $\pi\pi^*$ deloc.	A' 3.75 eV (0.1298) $\pi\pi^*$ (HOMO \rightarrow LUMO deloc.)	A' 4.19 eV (0.0030) $\pi\pi^*$ CT (Ph \rightarrow Tri)	A'' 3.20 eV (0.0045) $n\pi^*$ (n_N anti \rightarrow LUMO localized)	A' 3.40 eV (0.0908) $\pi\pi^*$ CT (Ph \rightarrow Tri)	A'' 3.19 eV (0.0043) $n\pi^*$ (n_N anti \rightarrow LUMO localized)	A' 3.98 eV (0.0681) $\pi\pi^*$ CT (Ph \rightarrow Tri)	A' 4.11 eV (0.0215) $\pi\pi^*$ CT (Ph \rightarrow Tri)	A' 2.48 eV (0.0005) $\pi\pi^*$ CT (Ph \rightarrow Tri) Tri HOMO \rightarrow LUMO
S ₃	A'' 4.32 eV (0.0005) $(n_N$ anti \rightarrow LUMO deloc.)	A' 4.35 eV (0.0035) $(n_N$ anti \rightarrow LUMO + 1 localized Tri)	A' 4.28 eV (0.0027) $n\pi^*$ (n_N/n_O \rightarrow LUMO deloc.)	A' 3.64 eV (0.1107) $\pi\pi^*$ CT (Ph \rightarrow Tri)	A'' 3.84 eV (0.0001) $n\pi^*$ (n_N anti \rightarrow LUMO + 1 localized Tri)	A' 3.74 eV (0.1109) $\pi\pi^*$ CT (Ph \rightarrow Tri)	A' 4.01 eV (0.0034) $n\pi^*$ (n_N anti \rightarrow localized)	A' 4.66 eV (0.2905) $\pi\pi^*$ deloc.	A' 3.23 eV (0.0000) $n\pi^*$ (n_N anti \rightarrow LUMO + 1 deloc.)
S ₄	A' 4.52 eV (0.0065) $(n_N$ anti \rightarrow LUMO + 1 localized Tri)	A' 4.41 eV (0.0005) $n\pi^*$ (n_N anti \rightarrow LUMO deloc.)	A' 4.63 eV (0.3355) $\pi\pi^*$ deloc.	A' 3.80 eV (0.0000) $n\pi^*$ (n_N anti \rightarrow LUMO + 1 deloc.)	A' 4.06 eV (0.0147) $\pi\pi^*$ CT (Ph \rightarrow Tri)	A' 3.80 eV (0.0002) $n\pi^*$ (n_N anti \rightarrow LUMO + 1 deloc.)	A' 4.36 eV (0.2329) $\pi\pi^*$ deloc.	A' 4.86 eV (0.0011) $n\pi^*$ (n_N/n_O \rightarrow LUMO deloc.)	A' 3.35 eV (0.0057) $\pi\pi^*$ CT (Ph \rightarrow Tri)

characterization of the states are given in Table 1. This study has two objectives. First, we use these computations to document the nature of the states being populated in the vertical region of the enol form. Second, we would like to transfer our detailed CASSCF results to *o*-hydroxyphenyl-(1,3,5)-triazine (R^1) and *o*-hydroxyphenyl-(1,2,4)-triazine (R^5) to the other systems not studied at the CASSCF level.

From Table 1, one can see that in all the triazine systems (R^1 , R^4 , R^5 , and R^6 in Chart 2), the lowest two $\pi\pi^*$ -transitions are of CT character although they differ in oscillator strengths. In the molecules under consideration, one would expect any CT transition to have appreciable oscillator strength. However, comparison with the CASSCF results shows that in the locally excited state, there is a small degree of charge transfer from the phenyl to the triazine ring (around 0.3 electrons). This is not enough for the state to be classified as a CT state but does show up in some of the TD-DFT states. We can use the oscillator strengths to compare the relative ordering of the CT and LE states. In the CT state, significant electronic density is transferred from the phenyl group to the triazine ring. This is in agreement with our detailed study of *o*-hydroxyphenyl-(1,3,5)-triazine (R^1) and the R^5 *o*-hydroxyphenyl-(1,2,4)-triazine discussed in the next section, using the spin-exchange density to characterize the nature of the states, where we observe that around 0.6 electrons is transferred in the S_2 state at the CASSCF level.

It should be noted that the optically active CT state and the valence tautomeric state (the LE state) are the first two $\pi\pi^*$ -states in all of the systems studied and are quite close in energy in all chromophores. In addition, the ordering of the CT and LE states differs depending on the particular chromophore. Since TD-DFT is known to give unreliable energetics for CT states, while CASSCF state orderings between covalent and ionic states are frequently reversed, deactivation from both of these states should be considered as we discuss later. However, our detailed wave function analysis for *o*-hydroxyphenyl-(1,3,5)-triazine (R^1) and *o*-hydroxyphenyl-(1,2,4)-triazine (R^5) suggests that all the *o*-hydroxyphenyl-triazines should undergo a very similar photostability mechanism since either the CT or LE state pathways lead to efficient regeneration of the ground-state enol form.

We now discuss the detailed documentation that underpins the cartoon of the potential energy surface shown in Figure 4 as well as the VB structures shown in Figure 3. All geometry optimizations were carried out at the CASSCF level, and the details are given in the computational details section. The energetics are gathered in Table 2, and the optimized geometrical parameters are in Table 3. Cartesian coordinates of all optimized geometries are given as Supporting Information. The information used to derive the valence-bond structures shown in Figure 3 is given in Tables 4 and 5. Finally, the characterization of the optimized critical points for the S_0/S_1 conical intersection seam is given in Figures 6 and 7, while the corresponding information for the S_1/S_2 conical intersection is collected in Figures 8 and 9.

Let us begin with a very brief discussion of the valence-bond resonance structures of the excited states involved along the reaction coordinate between the enol and the keto form. The information that is used to construct the valence-bond structures shown in Figure 3 is obtained from the orbital densities and spin-exchange densities of the vertically excited enol and keto states given in Tables 4 and 5. For example, by summing the one-electron densities shown in Table 4, one can see that the enol S_1 vertical $6\pi:8\pi$ state correlates diabatically with the keto S_2 $6\pi:8\pi$ CT state, and similarly, the keto S_1 vertical $7\pi:7\pi$

TABLE 2: *o*-Hydroxyphenyl-(1,3,5)-triazine CASSCF/6-31G* Energetics^a

geometry	adiabatic state	active space	energy (au)	relative energy (to S_0 min)/kcal mol ⁻¹
enol (planar)	S_0 - minimum	(12,11)	-583.23925	0.0
	S_1 - V	(12,11)	-583.26120	102.1
	S_2 - V	(12,11)	-583.09850	120.5
ground-state proton-transfer transition state	S_0 - TS	(12,11)	-583.06918	26.9
	S_1 - V	(12,11)	-583.06220	111.1
	S_2 - V	(12,11)	-583.04462	122.1
	S_0 - minimum	(12,11)	-583.21206	23.1
	S_1 - V	(12,11)	-583.07634	47.6
keto (planar)	S_2 - V	(12,11)	-583.18541	112.9
	S_1 - V	(14,13)	-583.08118	99.8
enol (planar)	S_0 - V	(12,11)	-583.08021	20.4
	S_1 - minimum	(12,11)	-583.20669	77.3
keto (planar)	S_0 - V	(12,11)	-583.11595	49.4
	S_1 - minimum (state averaged)	(12,11)	-583.16050	110.0
S_0/S_1 conical intersection on enol side	S_0/S_1	(12,11)	-583.06396	82.6
S_0/S_1 conical intersection on keto side	S_0/S_1	(12,11)	-583.10766	102.3
S_1/S_2 conical intersection on keto side	S_1/S_2	(12,11)	-583.07622	

^a V = vertical.

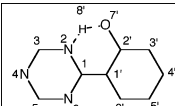
state correlates diabatically with the enol CT $7\pi:7\pi$ S_2 state. The assignment of the VB structures is discussed in the Computational Details section.

The relative energetics of the critical points summarized in Table 2 and the optimized geometries shown in Table 3 provide the data that underpin the cartoon of the potential surface shown in Figure 4. Notice that the keto form of the triazine is predicted to have a stable ground-state minimum (this is true for all species

shown in Chart 2). The fact that a stable ground-state keto species exists is an important difference between triazines and BZT. One might be tempted to think that the existence of this (new chemical) species would have a detrimental affect on photostability. However, we have optimized the transition state for proton transfer on S_0 , and the barrier from the keto minimum is only 3.8 kcal mol⁻¹ (Table 2).

As we have briefly discussed previously, from the valence-bond structures shown in Figure 3, it is clear that both the S_0/S_1 and the S_1/S_2 crossing seams are coupled by skeletal motion rather than by a coordinate corresponding to hydrogen migration. Thus, for example, the electronic structure of S_2 at the enol geometry differs from that of S_1 only in the coupling of the π -electrons. A detailed documentation of the two crossing seams is contained in Table 2 (energetics), in Table 3 (geometries), and in Figures 6–9, where the gradient difference and derivative coupling vectors that lift the degeneracy at the conical intersection are shown together with the gradients of the states involved. As an example, let us compare the information in Figure 6 (the enol S_0/S_1 conical intersection) with the valence-bond structures shown in Figure 3. First, notice (Figure 3) that at the enol form, the S_0 and S_1 valence-bond structures are valence tautomers, with a different spin coupling of the π -electrons. In correspondence with this, the derivative coupling and gradient difference vectors involve skeletal deformation. Notice in particular that in Figure 6a, the gradient difference vector has a component of the inter-ring C–C stretch, which is in agreement with the increase of the P_{ij} element on that bond upon excitation. In Figure 6c,d, we show the gradients for the S_0 and S_1 states. Notice that the gradients are essentially parallel and that this is the signature of a sloped intersection. (This has also been verified by means of an IRC from a slightly displaced geometry from the intersection; the IRC leading to the S_1 minimum). It is clear, on looking at Figure 7, that the analogous situation occurs at the keto geometry. The intersection at the enol side is 10 kcal mol⁻¹ above the S_1 enol minimum and can be accessed via out-of-plane bending motion. The keto intersection geometry is almost planar, with only a small deviation from planarity, and lies only some 5 kcal mol⁻¹ above the S_1 keto minimum. The different decay pathways for the keto forms of

TABLE 3: Optimized Geometries for *o*-Hydroxyphenyl-(1,3,5)-Triazine^{a,b}

	S_0 enol minimum ^c	S_0 Transition State ^c	S_0 keto minimum ^c	S_1 enol minimum ^c (planar)	S_1 keto minimum ^{c,d} (planar)	S_0/S_1 enol conical intersection ^{c,d}	S_0/S_1 keto conical intersection ^{c,d}	S_1/S_2 keto conical intersection ^{c,d,e}
1 - 2	1.34	1.33	1.36	1.36	1.35	1.44	1.34	1.33
2 - 3	1.33	1.34	1.36	1.32	1.37	1.29	1.37	1.32
3 - 4	1.32	1.29	1.28	1.33	1.35	1.44	1.41	1.36
4 - 5	1.33	1.36	1.39	1.35	1.29	1.29	1.26	1.35
5 - 6	1.32	1.30	1.28	1.31	1.41	1.42	1.41	1.29
1 - 6	1.34	1.37	1.39	1.36	1.29	1.40	1.29	1.42
1 - 1'	1.48	1.42	1.37	1.42	1.49	1.43	1.51	1.47
1' - 2'	1.39	1.43	1.47	1.44	1.46	1.43	1.46	1.47
2' - 3'	1.41	1.44	1.47	1.43	1.46	1.38	1.47	1.42
3' - 4'	1.39	1.36	1.35	1.42	1.36	1.39	1.37	1.43
4' - 5'	1.40	1.43	1.45	1.39	1.43	1.38	1.45	1.35
5' - 6'	1.38	1.35	1.35	1.44	1.36	1.40	1.35	1.46
1' - 6'	1.42	1.43	1.46	1.41	1.42	1.40	1.44	1.36
2' - 7'	1.34	1.27	1.23	1.31	1.24	1.34	1.26	1.23
7' - 8'	0.95	1.29	1.85	0.97	1.93	0.94	2.16	1.77
2 - 8'	1.88	1.17	1.00	1.78	0.99	2.01	0.99	1.03
1' - 1 - 4 angle	180.0°	180.0°	180.0°	180.0°	180.0°	103.9°	168.1°	172.9°
2' - 1' - 1 - 6 dihedral angle	180.0°	180.0°	180.0°	180.0°	180.0°	-165.1°	-161.5°	165.0°
2' - 1' - 1 - 2 dihedral angle	0.0°	0.0°	0.0°	0.0°	0.0°	-26.9°	21.7°	-3.9°

^a All bond lengths in angstroms. ^b 6-31G* basis in all computations. ^c (12,11) active space. ^d Uncorrected state-averaged gradient used (orbital rotation derivatives equal to zero). ^e S_1/S_2 state averaging.

TABLE 4: Localized One-Electron Density Matrix Elements (D_{ii}) for *o*-Hydroxyphenyl-(1,3,5)-Triazine

	S_0 enol minimum	S_1 enol vertical	S_1 enol minimum	S_2 enol vertical	S_0 keto minimum	S_1 keto vertical	S_1 keto minimum	S_2 keto vertical
1	0.841	0.951	0.981	0.984	0.935	0.837	0.878	0.975
2	1.206	1.243	1.259	1.504	1.674	1.532	1.589	1.482
3	0.845	0.851	0.851	0.927	0.856	1.076	1.074	0.930
4	1.166	1.221	1.234	1.091	1.226	1.118	1.153	1.248
5	0.843	0.848	0.853	0.957	0.866	1.016	0.920	0.831
6	1.167	1.195	1.196	1.120	1.153	1.415	1.332	0.975
1'	1.101	1.021	1.024	0.987	1.144	1.006	1.031	1.042
2'	0.921	0.899	0.876	0.905	0.789	0.826	0.829	0.878
3'	1.041	1.006	0.994	1.036	1.035	1.004	0.999	1.058
4'	0.966	1.036	1.035	0.935	0.952	0.968	0.972	0.978
5'	1.034	0.933	0.935	1.018	1.034	0.962	0.966	1.030
6'	0.967	0.978	0.965	0.958	0.981	0.958	0.962	0.896
7'	1.903	1.819	1.797	1.578	1.356	1.282	1.294	1.677

TABLE 5: Spin-Exchange Density Matrix Elements (P_{ij}) for *o*-Hydroxyphenyl-(1,3,5)-Triazine

	S_0 enol minimum	S_1 enol vertical	S_1 enol minimum	S_2 enol vertical	S_0 keto minimum	S_1 keto vertical	S_1 keto minimum	S_2 keto vertical
1 - 2	0.290	0.213	0.192	0.147	0.086	0.208	0.155	0.202
2 - 3	0.320	0.340	0.334	0.222	0.116	0.125	0.112	0.197
3 - 4	0.331	0.297	0.299	0.295	0.493	0.338	0.200	0.309
4 - 5	0.301	0.054	0.239	0.324	0.092	0.381	0.488	0.158
5 - 6	0.350	0.374	0.397	0.213	0.566	0.069	0.039	0.433
1 - 6	0.277	0.202	0.173	0.237	0.079	0.248	0.365	0.114
1 - 1'	0.072	0.143	0.192	0.164	0.404	0.091	0.034	0.094
1' - 2'	0.289	0.074	0.063	0.205	0.075	0.114	0.120	0.120
2' - 3'	0.276	0.229	0.216	0.144	0.069	0.091	0.099	0.173
3' - 4'	0.370	0.286	0.300	0.356	0.574	0.538	0.501	0.303
4' - 5'	0.289	0.345	0.374	0.255	0.107	0.162	0.204	0.364
5' - 6'	0.376	0.222	0.215	0.408	0.564	0.427	0.368	0.207
1' - 6'	0.286	0.284	0.282	0.197	0.094	0.275	0.330	0.381
2' - 7'	0.048	0.084	0.102	0.062	0.479	-0.052	0.444	0.333

the BZT and triazine based stabilizers can be rationalized in terms of the different electronic states involved. The keto tautomer of the *o*-hydroxyphenyl-triazine, which is the subject of the present study, has a stable, closed-shell resonance structure (see Figure 3), and the excitation induces a recoupling of the conjugated p-system formed by the C3–N4, C5–N6, and C1–C1' bonds of the ground state form (see the changes in the bond lengths of the two keto minima in Table 3 and the changes of the corresponding P_{ij} elements in Table 5). Therefore, the gradient difference associated to the keto-side intersection, which is also the coordinate that leads from the S_1 minimum to the intersection, is the bond inversion coordinate of these bonds (see Figure 7). In contrast to this, in BZT there is no closed-shell structure for the keto tautomer, and the decay from S_1 to S_0 involves a different pair of states.

We have also been able to find S_0/S_1 crossing points in the region of the S_1 transition state. Thus, the computations show

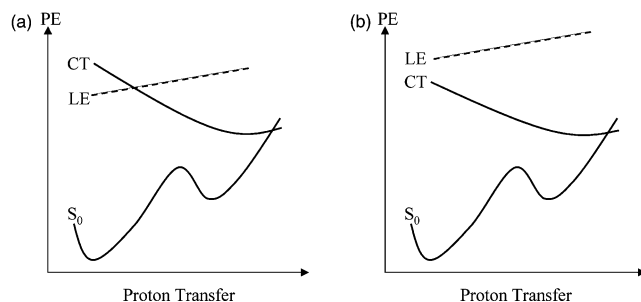


Figure 5. (a) Energy profiles along the reaction coordinate for different vertical excitation orderings. (a) Mechanism 1: lowest vertical local excitation (LE) with crossing along reaction coordinate and (b) mechanism 2: lowest vertical charge-transfer (CT) excitation.

an extended seam of crossing for the S_1 and S_0 states all along the proton transfer coordinate. Inspection of Figure 8 shows an analogous situation for typical geometry on the S_2/S_1 conical intersection (shown at the keto side).

It must be noted that in the region where the excited-state diabatic surfaces cross (central region in Figure 4), the branching space contains some component of the reaction coordinate (the proton transfer). Thus, the diabatic $6\pi:8\pi$ and $7\pi:7\pi$ surfaces interact in Figure 4 to produce an avoided crossing of the adiabatic surfaces. The branching space coordinates at a point on the S_1/S_2 CI seam are shown in Figure 9. This point was found by optimizing the energy difference by starting at the S_1 TS geometry. It can be seen from Figure 9a that the derivative coupling in this region contains a component of the NH stretching vibration, which is contained in the reaction path. However, as we discuss next, this has no mechanistic implications for photostability. The region where the excited-state diabats cross is very narrow, and as can be seen from Figure 4, the S_0/S_1 and S_1/S_2 seams of intersection are essentially parallel along the remaining part of the reaction path.

Before discussing the mechanistic implications of the computed potential energy surface data, we need to give careful consideration as to the theoretical limitations of our computations and the confidence that we may have in our data. The central issue relates to the ordering of the two $\pi\pi^*$ -states. We also need to recognize the errors inherent in the TD-DFT method (which can have difficulties with charge-transfer states) and in the CASSCF method (where the energies of ionic states are often underestimated due to dynamic correlation). There is also the issue that the ordering of the two $\pi\pi^*$ -states in triazines will vary with the specific nature of the triazine chromophore.

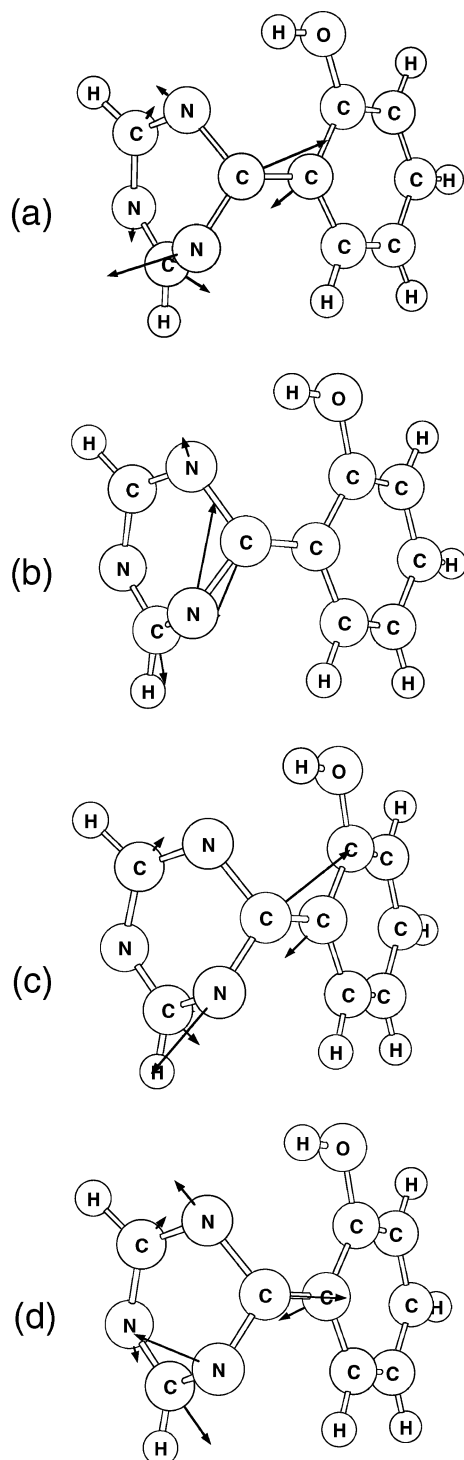


Figure 6. S_0/S_1 optimized conical intersection at the enol side. (a) Gradient difference vector, (b) derivative coupling vector, (c) S_0 gradient, and (d) S_1 gradient.

Let us compare the CASSCF vertical excitation energies (Table 2) with the TD-DFT results contained in column one of Table 1. For *o*-hydroxyphenyl-(1,3,5)-triazine, analysis of the CASSCF vertical excitations shows that S_1 is locally excited but that S_2 is a charge-transfer state and that the energy difference between the two states is approximately 0.7 eV. In contrast, the corresponding TD-DFT results show the states to be separated by only 0.3 eV with the charge-transfer state lower in energy. Thus, if we look along the proton transfer reaction coordinate, we cannot distinguish between the scenario shown in Figure 5a, which corresponds to our CASSCF computations,

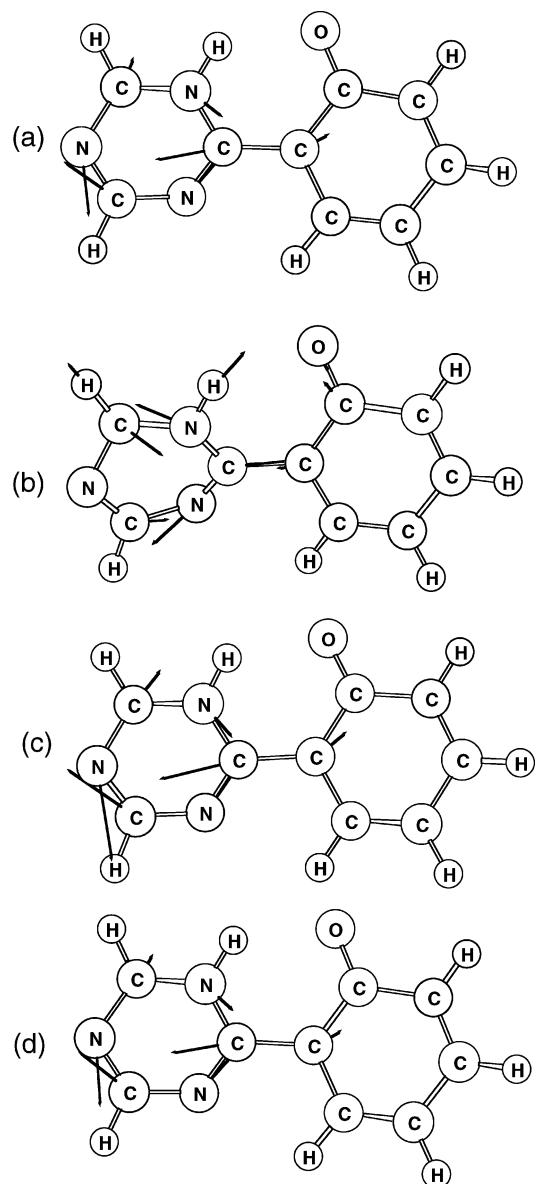


Figure 7. S_0/S_1 optimized conical intersection at keto side. (a) Gradient difference vector, (b) derivative coupling vector, (c) S_0 gradient, and (d) S_1 gradient.

and the alternative possibility shown in Figure 5b, which is the one suggested from the TD-DFT computations. Experimentally, however, it appears that the CT is S_1 .⁴

Let us examine the implications from a mechanistic point of view arising from the inability to distinguish with a high level of confidence between Figure 5a and Figure 5b. (Let us recognize that in the range of triazines presented in Chart 2 and Table 1, the relative ordering (TD-DFT) of the locally excited and charge-transfer states may change in any case.) It is clear that in both Figure 5a and Figure 5b, one has the prediction that in following photoexcitation to the enol charge-transfer state, the keto S_1 minimum will be reached without barrier because motion will occur on this single diabatic state (see also Figure 4). The only question, as shown in Figure 5a, is whether this process proceeds via a conical intersection or not. At the S_1 keto geometry, the existence of the extended S_0/S_1 conical intersection seam will be independent of the level computations. There remains the question of the interpretation of the S_0/S_1 conical intersection at the enol geometry. In our CASSCF results, this intersection is between two valence tautomers corresponding to recoupling of the π -electrons, and

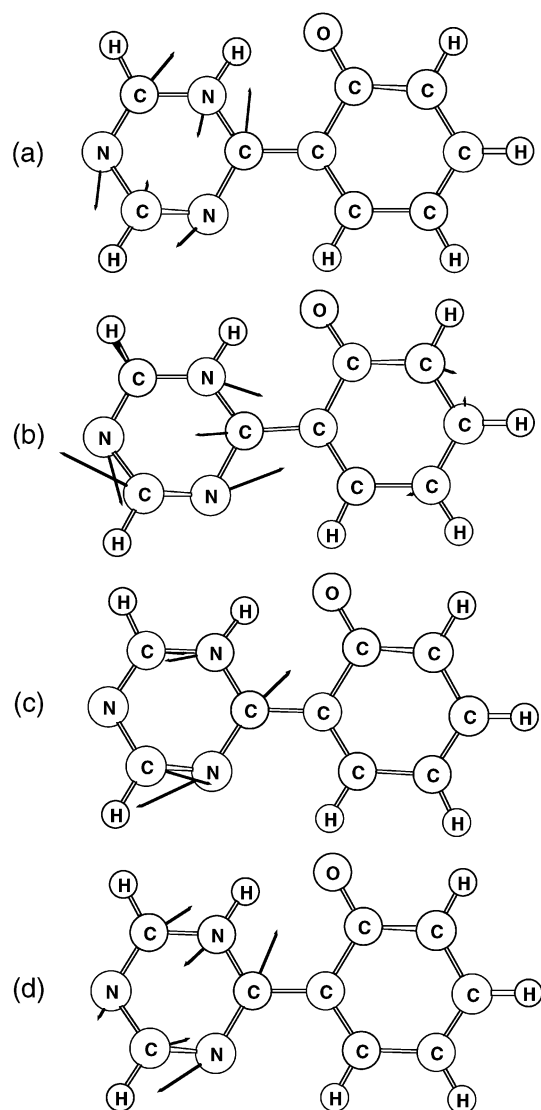


Figure 8. S_1/S_2 optimized conical intersection at keto side. (a) Gradient difference vector, (b) derivative coupling vector, (c) S_1 gradient, and (d) S_2 gradient.

as a consequence, the geometrical coordinates involved do not involve hydrogen motion. Now let us suppose that the situation is as shown in Figure 5b. In this case, the S_0/S_1 conical intersection at the enol geometry would involve a charge-transfer configuration and S_0 . However, this will simply be an extension of the conical intersection line in a direct way from the keto geometry. Further, the two electronic configurations involved differ only in the coupling of the π -electrons, so one expects that the conical intersection must be sloped as well (see the gradients in Figures 6–8).

In the preceding discussion, we have documented the main features of the surface topology shown in Figure 4, as well as documenting the electronic structure of excited states involved in Figure 3. The CASSCF results suggest that a seam of intersections is accessible along the entire reaction path. Furthermore, this seam has everywhere a first-order sloped topology, which is desirable in a photostabilizer. The valence-bond analysis suggests that the mechanistic ideas are independent of whether the lowest energy state is charge-transfer or locally excited.

The existence of an energetically accessible region of the seam, along the entire excited state reaction path, suggests that the triazine class of photostabilizers has the potential for

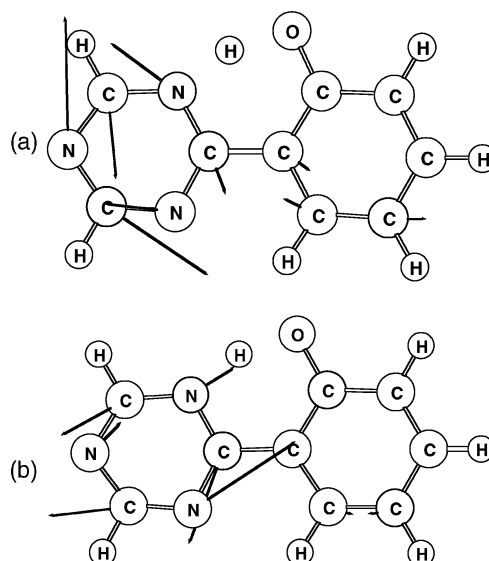


Figure 9. S_1/S_2 intersection point lying in the TS region. (a) Gradient difference vector and (b) derivative coupling vector, which has a component of the NH stretching vibration.

exceptional photostability. Radiationless decay at any point on the seam will inevitably lead to the regeneration of the ground-state enol species. This can either occur in a direct manner, with decay at the enol side, or after the ESIPT at the sloped conical intersection on the keto side (since the regeneration of the ground-state enol occurs with negligible barrier).

Conclusions

We have studied the ESIPT mechanism in the *o*-hydroxyphenyl-triazine class of photostabilizers. Our results suggest that these compounds have the potential for excellent photostability due to two key mechanistic features: (1) the ESIPT reaction path is planar and involves the minimum amount of molecular motion and (2) an extended seam of conical intersections, parallel to the reaction path, allows for radiationless decay at any point along the path, even at the enol side. This explains experimental observations that the proton transfer is in competition with a temperature-dependent deactivation process.¹⁴ For photostability, this paradigm is ideal since the seam has everywhere a sloped topology and the ground-state enol form is regenerated on an ultrafast time scale. These mechanistic features are independent of the ordering of the locally excited versus charge-transfer configurations. The notion of a seam of intersection explains the high photostability of the *o*-hydroxyphenyl-triazine class of photostabilizers in particular, but more generally highlights an important photochemical feature that should be considered when designing a photostabilizer.

Acknowledgment. All computations were carried out on an IBM-SP2 funded jointly by IBM-UK and HEFCE (UK). Ciba Specialty Chemicals provided financial support for this project to M.J.P. and M.A.R. L.B. is financed by the Ramón y Cajal program from the Spanish Ministerio de Ciencia y Tecnología and by Grants BQU200204112-C02-02 and BZ2002-03334 from the Spanish Dirección General de Enseñanza Superior e Investigación Científica y Técnica (MECD).

Supporting Information Available: Cartesian coordinates of all optimized geometries given in Table 3. This material is available free of charge via the Internet at <http://pubs.acs.org>.

References and Notes

- (1) Leppard, D.; Hayoz, P.; Schäfer, T.; Vogel, T.; Wendeborn, F. *Chimia* **2002**, *56*, 216.
- (2) Paterson, M. J.; Robb, M. A.; Blancafort, L.; De Bellis, A. *J. Am. Chem. Soc.* **2004**, *126*, 2912.
- (3) Atchity, G. J.; Xantheas, S. S.; Ruedenberg, K. *J. Chem. Phys.* **1991**, *95*, 1862.
- (4) Keck, J.; Kramer, H. E. A.; Port, H.; Hirsch, T.; Fischer, P.; Rytz, G. *J. Phys. Chem.* **1996**, *100*, 14468.
- (5) Elbe, F.; Keck, J.; Fluegge, A. P.; Kramer, H. E. A.; Fischer, P.; Hayoz, P.; Leppard, D.; Rytz, G.; Kaim, W.; Ketterle, M. *J. Phys. Chem. A* **2000**, *104*, 8296.
- (6) Waiblinger, F.; Keck, J.; Stein, M.; Fluegge, A. P.; Kramer, H. E. A.; Leppard, D. *J. Phys. Chem. A* **2000**, *104*, 1100.
- (7) Bearpark, M. J.; Bernardi, F.; Olivucci, M.; Robb, M. A.; Smith, B. R. *J. Am. Chem. Soc.* **1996**, *118*, 5254.
- (8) Ismail, N.; Blancafort, L.; Olivucci, M.; Kohler, B.; Robb, M. A. *J. Am. Chem. Soc.* **2002**, *124*, 6818.
- (9) Frisch, M. J.; Trucks, G. W.; Schlegel, H. B.; Scuseria, G. E.; Robb, M. A.; Cheeseman, J. R.; Zakrzewski, V. G.; Montgomery, J. A.; Stratmann, R. E.; Burant, J. C.; Dapprich, S.; Millam, J. M.; Daniels, A. D.; Kudin, K. N.; Strain, M. C.; Farkas, O.; Tomasi, J.; Barone, V.; Cossi, M.; Cammi, R.; Mennucci, B.; Pomelli, C.; Adamo, C.; Clifford, S.; Ochterski, J.; Petersson, G. A.; Ayala, P. Y.; Cui, Q.; Morokuma, K.; Malick, D. K.; Rabuck, A. D.; Raghavachari, K.; Foresman, J. B.; Cioslowski, J.; Ortiz, J. V.; Stefanov, B. B.; Liu, G.; Liashenko, A.; Piskorz, P.; Komaromi, I.; Gomperts, R.; Martin, R. L.; Fox, D. J.; Keith, T.; Al-Laham, M. A.; Peng, C. Y.; Nanayakkara, A.; Gonzalez, C.; Challacombe, M.; Gill, P. M. W.; Johnson, B. G.; Chen, W.; Wong, M. W.; Andres, J. L.; Head-Gordon, M.; Replogle, E. S.; Pople, J. A. *Gaussian 99* (Revision C1); Pittsburgh, PA, 1999.
- (10) Stratmann, R. E.; Scuseria, G. E.; Frisch, M. J. *J. Chem. Phys.* **1998**, *109*, 8218.
- (11) Boys, S. F. *Rev. Mod. Phys.* **1960**, *32*, 296.
- (12) Blancafort, L.; Celani, P.; Bearpark, M. J.; Robb, M. A. *Theor. Chim. Acta* **2003**, *110*, 92.
- (13) Paterson, M. J.; Blancafort, L.; Wilsey, S.; Robb, M. A. *J. Phys. Chem. A* **2002**, *106*, 11431.
- (14) Stueber, G. J.; Kieninger, M.; Schettler, H.; Busch, W.; Goeller, B.; Franke, J.; Kramer, H. E. A.; Hoier, H.; Henkel, S.; Fischer, P.; Port, H.; Hirsch, T.; Rytz, G.; Birbaum, J.-L. *J. Phys. Chem.* **1995**, *99*, 10097.